Rigid arc-shaped ligands for the fabrication of dative B–N-bonded crystalline porous polymers

Yan-Fang Wang, [a,b,†] Youlie Cai, [a,b,†] Zhenglin Du, [a,b] Ding Xiao [a,b] Mengbin Wang, [a,b] Ming Liu, [a,b] and Guangfeng Li * [a,b]

[a]State Key Laboratory of Soil Pollution Control and Safety, Stoddart Institute of Molecular Science, Department of Chemistry, Zhejiang University, Hangzhou 310058, P. R. China.

[b]Key Laboratory of High-Performance Adhesion Functional Materials and Application Technology of Zhejiang, Zhejiang-Israel Joint Laboratory of Self-Assembling Functional Materials, ZJU-Hangzhou Global Scientific and Technological Innovation Center, Zhejiang University, Hangzhou 311215 P. R. China.

†Y.-F. Wang and Y. Cai contributed equally to this work.

*Corresponding authors. E-mail: guangfengli@zju.edu.cn

Table of Contents

1. Materials and Methods

1.1 Materials

All the reagents involved in this research were commercially available and used without further purification unless otherwise noted. Solvents were either employed as purchased or dried before use by standard laboratory procedures. Thin-layer chromatography (TLC) was carried out on 0.25 mm Yantai silica gel plates (60F−254). Column chromatography was performed on silica gel (200−300 mesh) as the stationary phase.

1.2 Nuclear Magnetic Resonance Spectroscopy

^{1}H, ^{13}C NMR were performed on Bruker Avance-600 NMR spectrometers. Chemical shifts are reported in ppm with residual solvents as the internal standards. The following abbreviations were used for signal multiplicities: s, singlet; d, doublet; dd, doublet of doublet; m, multiplet.

1.3 Scanning Electron Microscopy

The crystal samples were transferred onto silicon wafers and coated with gold nanoparticles. Scanning electron microscope (SEM) observations and energy dispersive spectrometry (EDS) experiments were carried out on a Verios G4 Field Emission scanning electron microscope combined with energy dispersive X-ray analysis.

1.4 Single Crystal X-ray Diffraction

Single crystal X-ray diffraction data were collected on a Hybrid Pixel Array Detector with Cu Kα radiation (λ = 1.54184 Å) at 200 K. The structures were solved by intrinsic phasing methods (SHELXT) and refined by full-matrix least squares on F^2 using SHELXL[1] in the OLEX2 program package.[2] All non-hydrogen atoms were

refined with anisotropic thermal parameters and the hydrogen atoms were fixed at calculated positions and refined by a riding mode. SQUEEZE routine implemented on PLATON[3] was used to remove electron densities corresponding to disordered solvent molecules in the crystal data.

1.5 Thermogravimetric Analysis

Thermogravimetric analysis (TGA) was carried out on a SDT Q600 thermogravimetric analyzer. The crystal samples were heated at a rate of 10 ℃/min under nitrogen.

1.6 B−N Bond Energy Calculation

The calculated structure was built from its single crystal structures. All-electron DFT calculations were carried out using the ORCA quantum chemistry software (Version 5.0.4).[4] The positions of the hydrogen atoms were optimized, and the other atoms were maintained unchanged in their respective positions. The B3LYP functional[5] and 6-31g(d) basis set[6] were employed for the DFT structural optimization calculations. The interaction between the **L4** and the **BDBB**, known as interaction energy (ΔE_{int}), can be calculated by the following relation[7]:

$$\Delta E_{int} = E_{adduct} - (E_{L4} + 2E_{BDBB})$$

where E_{adduct} was the singlet point energy of the fragment of **L4** and two **BDBB**, E_{L3} was the singlet point energy of **L4**, and $E_{\mathbf{BDBB}}$ was the singlet point energy of **BDBB**. Based on the above methods, the value of the B−N bond energy in the **CPP** was calculated as half of ΔE_{int}.

Electrostatic potential (ESP) analysis was performed by Multiwfn software.[8,9,10] The visualization of ESP was rendered by VMD.[11]

1.7 Gas Sorption Measurements

The freshly prepared sample of **CPP-a** (0.5 g) was exchanged by ethyl ether for

24 hours, and using the fresh ethyl ether to replace many times during this time. Then, crystals were activated by supercritical carbon dioxide activation. CO_2 and C_2H_2 adsorption isotherms were measured on Micromeritics ASAP 2460 surface area analyzer for **CPP-a**. As the center-controlled air condition was set up at 25 ℃, a water bath of 25 ℃ was used for adsorption isotherms at 298 K. The CO_2/C_2H_2 selectivity of **CPP-a** was estimated using the ideal adsorbed solution theory (IAST). The measured experimental data consists of the excess loadings (q^{ex}) of the pure components CO_2 and C_2H_2 for **CPP-a**, which could be converted to absolute loadings (q) as follows:

$$q = q^{ex} + \frac{pV_{pore}}{ZRT}$$

where Z is the compressibility factor. The Peng-Robinson equation was used to estimate the value of the compressibility factor and used to obtain the absolute loading. The dual-site Langmuir-Freundlich equation is used for fitting the isotherm data at 298 K.

$$n(P) = q1\frac{(k1 \times p)\text{^}n1}{1 + (k1 \times p)\text{^}n1} + q2\frac{(k2 \times p)\text{^}n2}{1 + (k2 \times p)\text{^}n2}$$

Here p is the pressure of the bulk gas at equilibrium with the adsorbed phase (Pa), n(P) is the adsorbed amount per mass of adsorbent (mmol/g), *k1, k2* are adsorption affinity constants for the two types of sites, respectively (Pa^{-1}). $q1$, $q2$ are the maximum adsorbed amounts (saturation capacities) for the first and second types of sites, respectively (mmol g^{-1}). They represent the maximum amount of adsorbate that can be adsorbed when each type of site is fully occupied. $n1$, $n2$ are heterogeneity factors for the two types of sites, dimensionless parameters that describe the energy distribution uniformity of the adsorption sites. A value of 1 indicates homogeneous sites (degenerating to Langmuir behavior for that site), while deviations from 1 indicate heterogeneous energy distributions.

The adsorption selectivity for the different gases separation is defined by

$$S = \frac{q_1/q_2}{p_1/p_2}$$

where q_1 and q_2 are the molar loadings in the adsorbed phase in equilibrium with the bulk gas phase at partial pressures p_1 and p_2, respectively. The values of q_1 and q_2 were calculated using the Ideal Adsorbed Solution Theory (IAST) of Myers and Prausnitz[12].

1.9 Column Breakthrough Experiments

The breakthrough experiments for C_2H_2/CO_2 mixtures were carried out at BSD-MAB with a flow rate of 2 mL min^{-1} at temperatures of 298 K and pressures of 1 bar. In the separation experiment, activated samples (1 g) were packed into a $\Phi = 6 \times 110$ mm fixed-bed column, and the column was heated at 373 K for 2 hours before testing. In the desorption process, samples were activated at vacuum (1×10^{-6} bar) or by flushing the adsorption bed with helium (50 mL min^{-1}) for 60 min at 298 K.

1.10 Powder X-ray diffraction Experiments

Powder X-ray diffraction (PXRD) was carried out with a SmartLab SE powder diffractometer equipped with a Cu sealed tube (λ = 1.54184 Å) at 40 kV and 40 mA over the 2θ range of 5−50°.

1.11 Grand Canonical Monte Carlo (GCMC) simulations

Grand Canonical Monte Carlo (GCMC) simulations[13] of **CPP-a** were performed using the sorption module. During the simulation, the framework, C_2H_2, and CO_2 are considered rigid. The simulations were carried out at 298 K, adopting the fixed pressure task, Metropolis method, and the Dreiding field.[14] The framework used the 2 × 1 × 1 cell. The interaction energy between gas molecules and framework were computed through the Coulomb and Lennard-Jones (LJ) potentials. The cutoff radius was chosen as 15.5 Å for the LJ potential and the long-range electrostatic interactions were handled using the Ewald summation method,[15] the summation method for van der Waals interactions is atom based. The loading step, equilibration step and production step are all 1×10^6.

The guest molecules were modeled using the TraPPE (Transferable Potentials for

Phase Equilibria) force field,[16] which is widely accepted for accurately reproducing the vapor-liquid equilibrium data of these gases.

The grand canonical Monte Carlo (GCMC) simulations were performed in the *NVT* ensemble to calculate the isosteric heats of adsorption Q_{st}. The internal energy ΔU was computed during the simulation, which is directly related to Q_{st}. The isosteric heat of adsorption Q_{st} was calculated from:

$$Q_{st} = RT - \frac{\langle U_{ff}N\rangle - \langle U_{ff}\rangle\langle N\rangle}{\langle N^2\rangle - \langle N\rangle\langle N\rangle} - \frac{\langle U_{sf}N\rangle - \langle U_{sf}\rangle\langle N\rangle}{\langle N^2\rangle - \langle N\rangle\langle N\rangle}$$

where R is the gas constant, N is the number of molecules adsorbed, and $\langle\ \rangle$ indicates the ensemble average. The U_{ff} in the first and second terms are the contributions from the molecular thermal energy and adsorbate-adsorbate interaction energy, respectively. The U_{sf} in the third term is the contribution from the adsorbent−adsorbate interaction energy.

The ESP charge of the effective fragment of the framework and guest molecules were calculated using the DMol3[15] module.[17] The Generalized Gradient Approximation (GGA) with the Perdew-Burke-Ernzerhof (PBE) functional was used to perform all-electron spin-unrestricted DFT calculations.[18] A semiempirical addition (the TS method) of dispersive forces to the conventional DFT was included in the calculation to account for van der Waals interactions. The energy, force and displacement convergence criterions were set as 1×10^{-5} Ha, 2×10^{-3} Ha and 5×10^{-3} Å, respectively. The double numerical including polarization (DNP) basis set was chosen for all atoms. To accelerate convergence, an SCF tolerance value of 1.0 e^{-6} and a smearing value of 0.05 Ha were used.

2. *Design Concept of the Research Project*

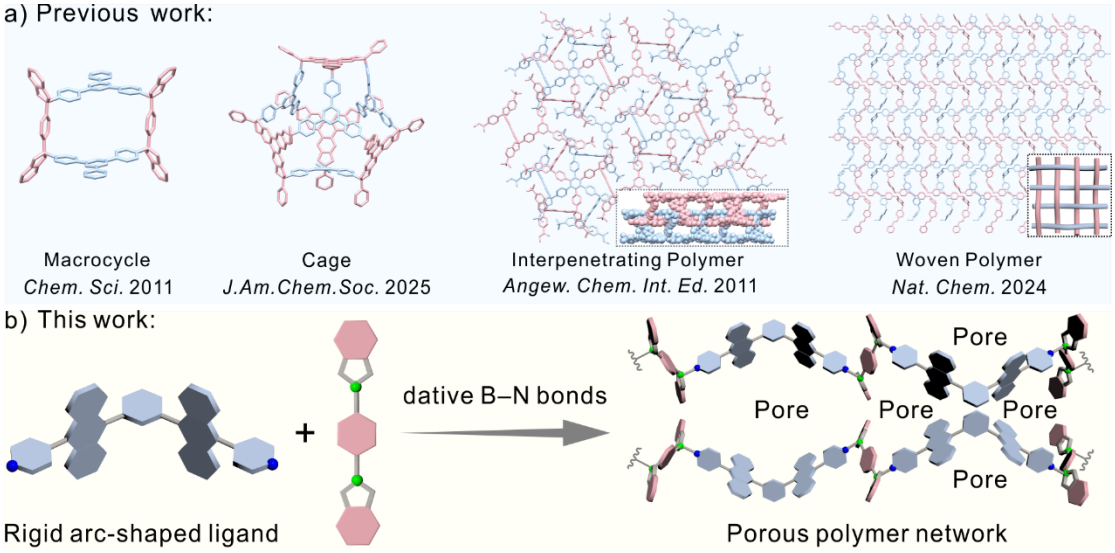

Fig. S1. (a) Architectures reported in previous works: macrocycle, cage, interpenetrating polymer, and woven polymer. (b) Schematic of this work: rigid arc-shaped ligands assembles with borate esters *via* dative B−N bonds, yielding a porous polymer network with well-defined pores.

3. Synthetic Protocols

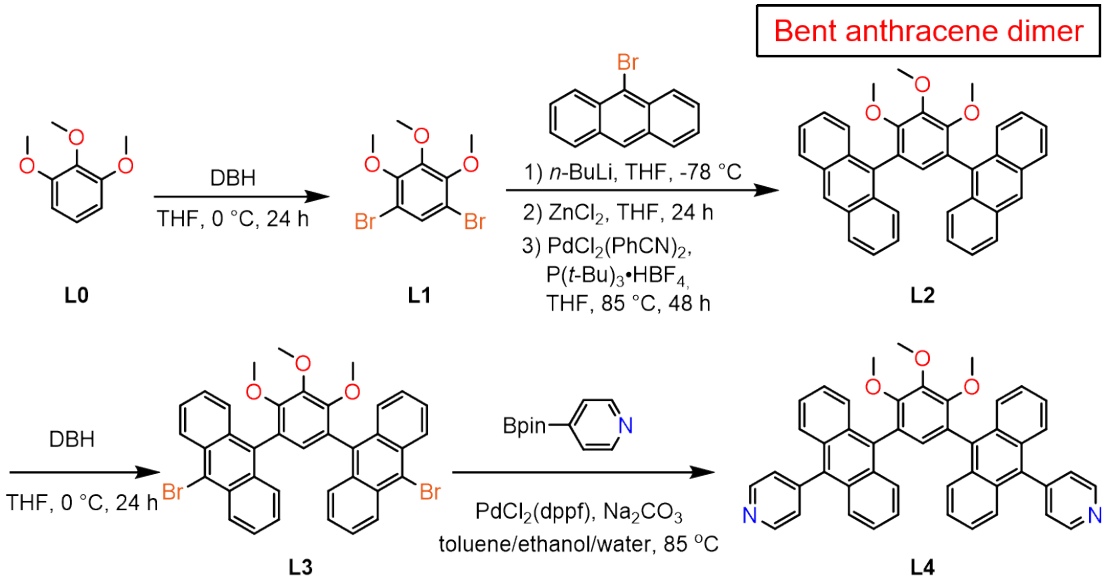

Fig. S2. The synthetic route of **L4**.

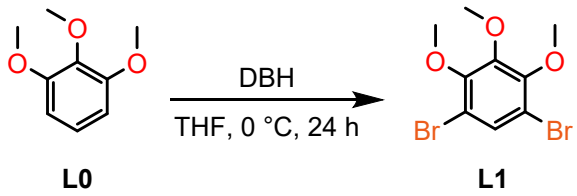

*Synthesis of compound **L1***: 1,2,3-Trimethoxybenzene (16.80 g, 100 mmol) and THF (150 mL) were added to a 500 mL round-bottom flask. To this stirred solution, a 150 mL THF solution of 1,3-dibromo-5,5-dimethylhydantoin (DBH; 42.89 g, 150 mmol) was slowly added at 0 ºC. The resulting mixture was then stirred at room temperature for 24 hours. After completion of the reaction, the mixture was poured into an aqueous sodium bisulfite solution, and the crude product was extracted with diethyl ether (3 × 50 mL). The combined organic extracts were washed with saturated brine, dried over anhydrous $MgSO_4$, filtered, and concentrated under reduced pressure. The crude residue was further purified by distillation to afford **L1** as a colorless oil (28.653 g, 88% yield). ^{1}H NMR (500 MHz, $CDCl_3$) δ (ppm): 7.48 (s, 1H), 3.93 (s, 3H), 3.89 (s, 6H). ^{13}C NMR (126 MHz, $CDCl_3$) δ (ppm): 151.08, 148.55, 129.96, 112.47, 61.52, 61.24. APCI-HRMS: *m/z* calcd for $[M]^+$ $C_9H_{10}Br_2O_3^+$, 325.8971, found 325.8970, error −0.3 ppm.

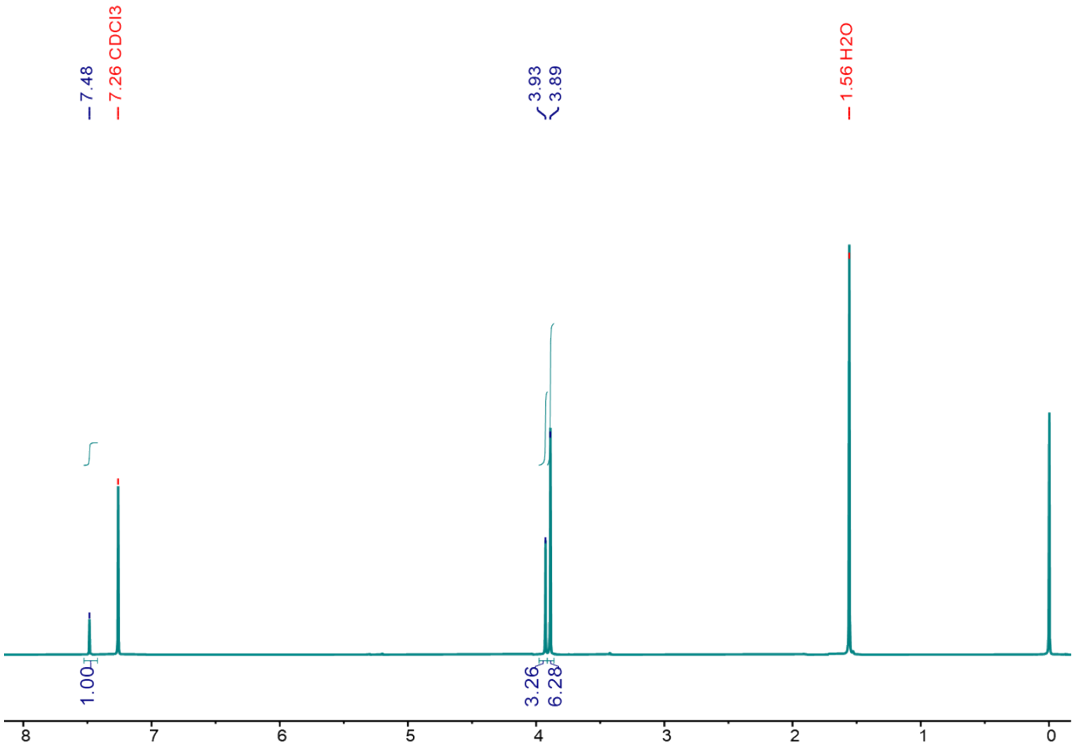

Fig. S3. The ^{1}H NMR spectrum (500 MHz, $CDCl_3$, 298 K) of **L1**.

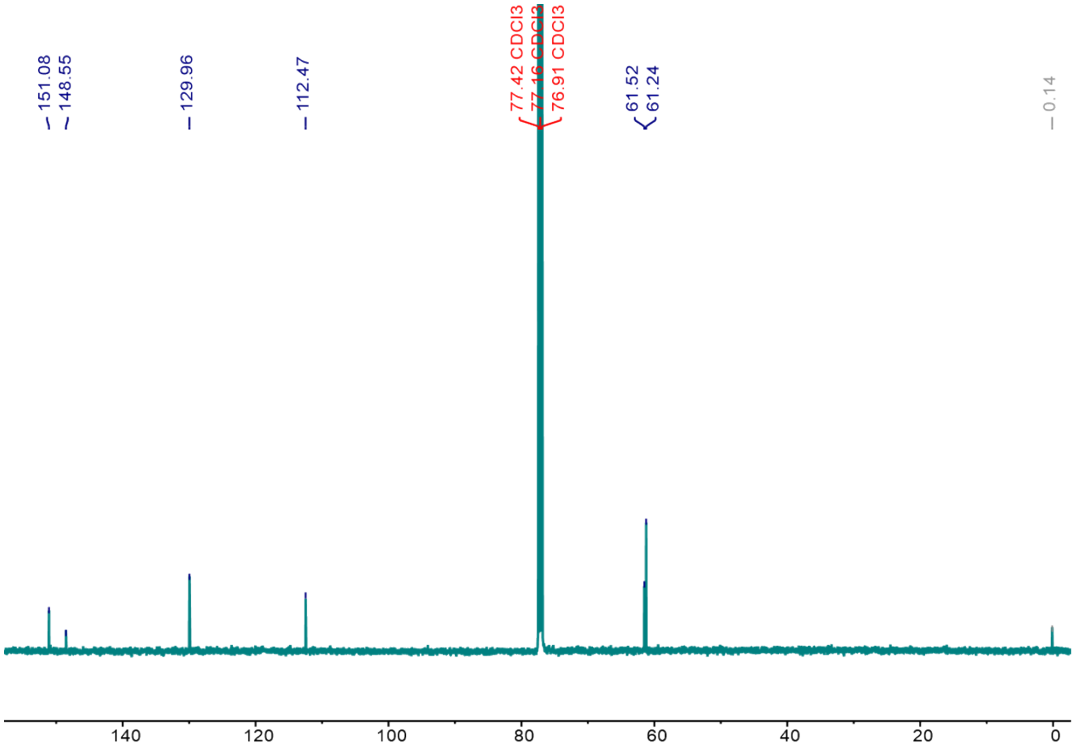

Fig. S4. The ^{13}C NMR spectrum (151 MHz, $CDCl_3$, 298 K) of **L1**.

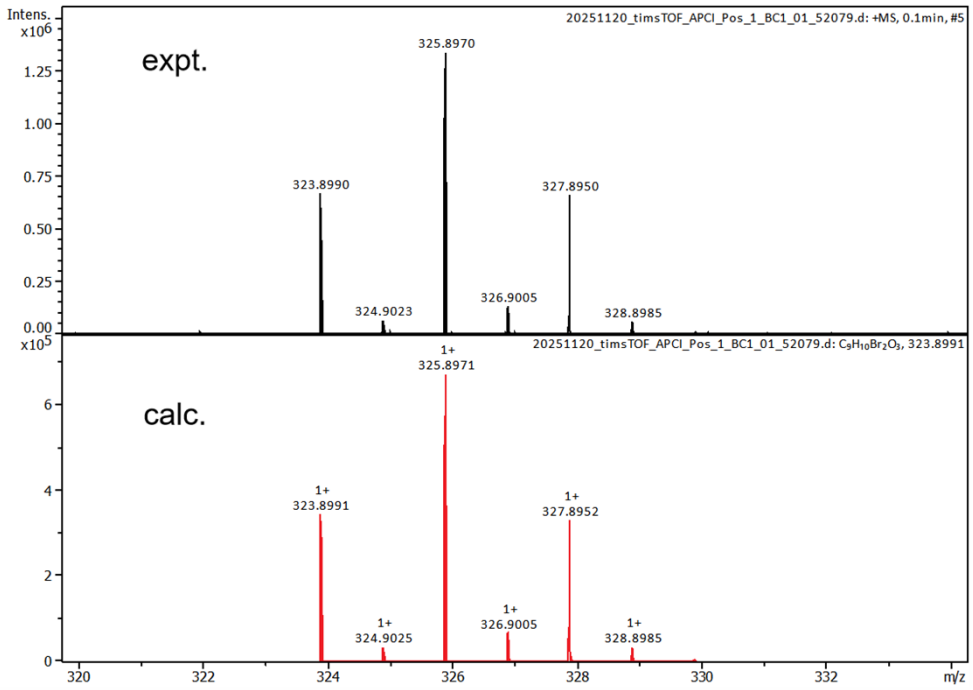

Fig. S5. APCI mass spectrum of **L1**.

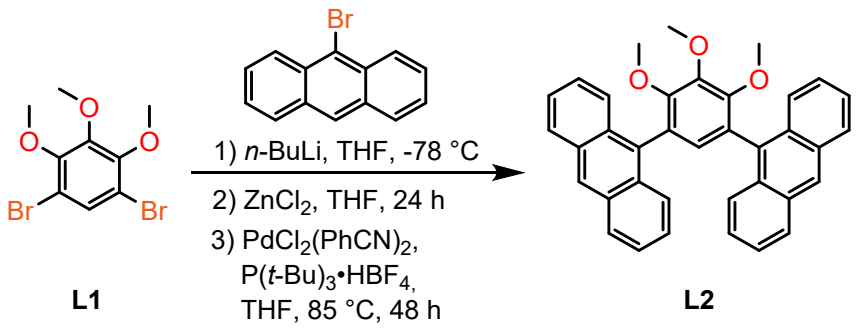

Synthesis of compound ***L2***: 9-Bromoanthracene (38.57 g, 150 mmol) and anhydrous THF (250 mL) were added to a 1 L three-necked round-bottom flask, which was purged with nitrogen and maintained under a N_2 atmosphere. A 6 M hexane solution of *n*-BuLi (26.7 mL, 160 mmol) was added dropwise via a syringe to the flask at −78 ºC under N_2 protection. Following stirring at −78 ºC for 2 h, a solution of anhydrous $ZnCl_2$ (27.26 g, 200 mmol) in anhydrous THF (150 mL) was slowly added to the reaction mixture. The resulting mixture was further stirred at −78 ºC for 1 h, then allowed to warm to room temperature and stirred for an additional 24 hours to in situ generate 9-anthrylzinc chloride. Separately, a round-bottom flask equipped with a

magnetic stir bar was purged with N_2. To this flask were added **L1** (16.30 g, 50 mmol), bis(benzonitrile)palladium(II) chloride ($PdCl_2(PhCN)_2$; 1.15 g, 3 mmol), and anhydrous THF (150 mL). A 0.96 M hexane solution of $P(t\text{-}Bu)_3$ (6.3 mL, 6 mmol) was added to the flask, and the mixture was stirred at r.t. for 30 min to activate the palladium catalyst. This pre-activated catalyst mixture was then transferred to the 1 L three-necked flask containing the 9-anthrylzinc chloride solution. The combined reaction mixture was heated to 85 ºC and stirred for 48 hours. After cooling to r.t., the precipitated crude solid was collected by vacuum filtration, sequentially washed with methanol and hexane to remove impurities, and dried under reduced pressure. This afforded **L2** as a white solid (15.621 g, 60% yield). ^{1}H NMR (500 MHz, $CDCl_3$) δ (ppm): 8.48 (s, 2H), 8.07–7.99 (m, 4H), 7.95–7.86 (m, 4H), 7.52–7.41 (m, 8H), 6.97 (s, 1H), 4.15 (s, 3H), 3.52 (s, 6H). ^{13}C NMR (126 MHz, $CDCl_3$) δ (ppm): 152.73, 146.84, 132.99, 131.53, 130.67, 130.63, 128.63, 127.72, 127.00, 126.72, 125.76, 125.21, 61.60, 61.26. APCI-HRMS: *m/z* calcd for $[M + H]^+$ $C_{37}H_{29}O_3^+$, 521.2111, found 521.2112, error 0.2 ppm.

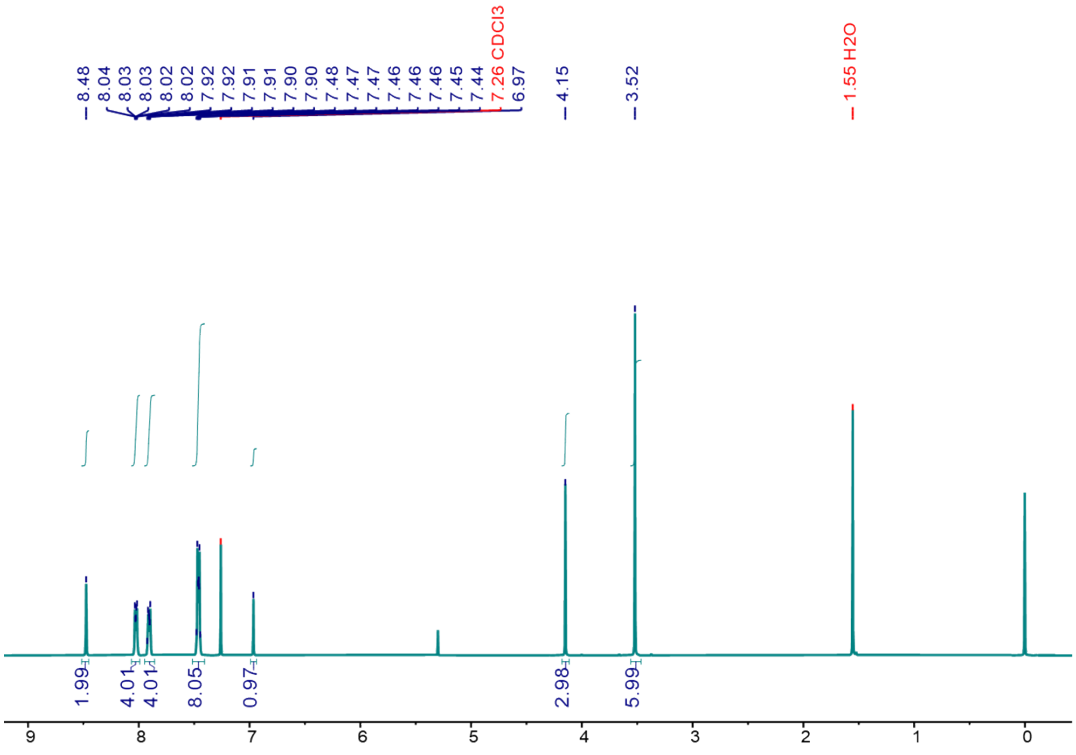

Fig. S6. The ^{1}H NMR spectrum (500 MHz, $CDCl_3$, 298 K) of **L2**.

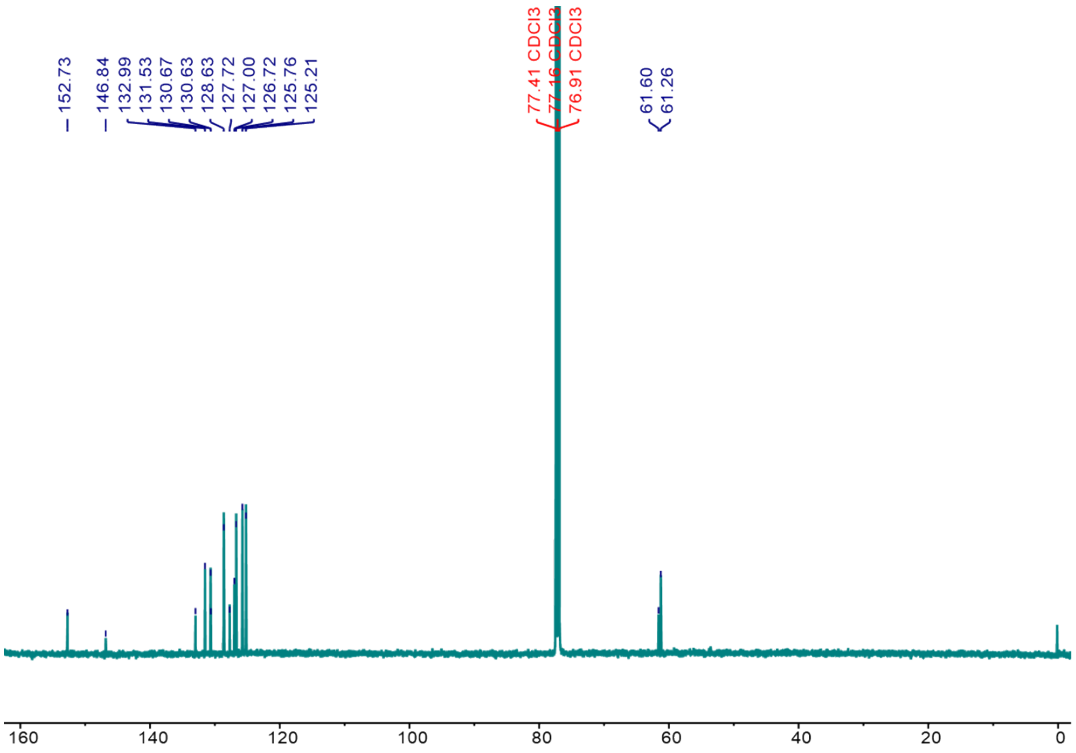

Fig. S7. The ^{13}C NMR spectrum (151 MHz, $CDCl_3$, 298 K) of **L2**.

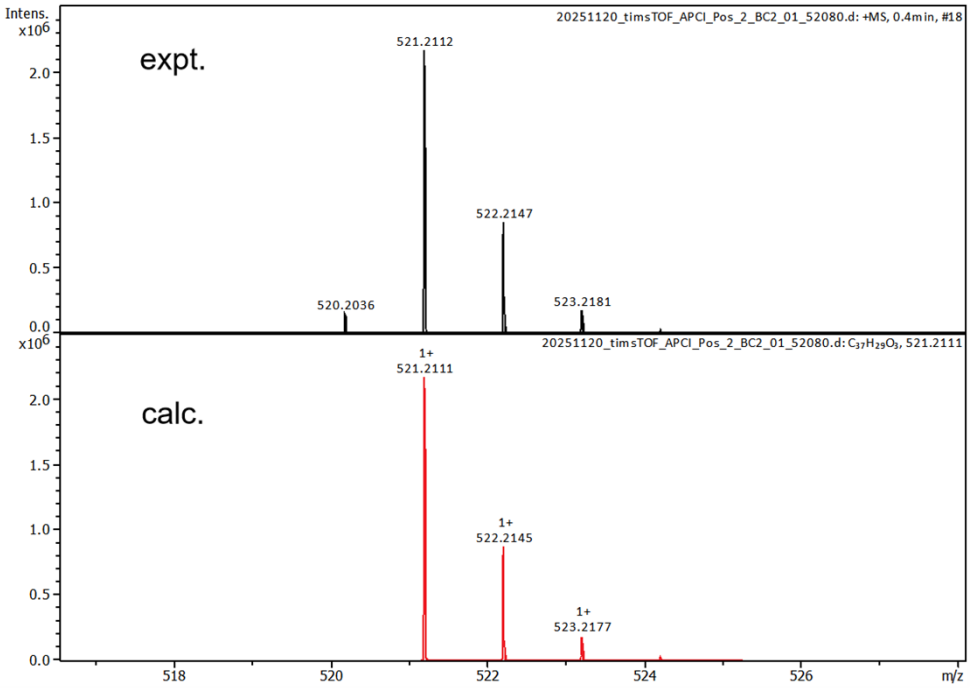

Fig. S8. APCI mass spectrum of **L2**.

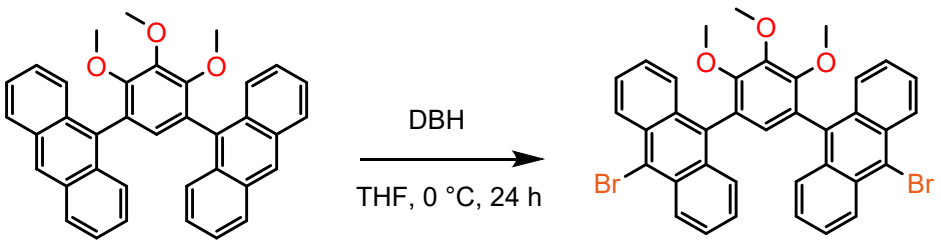

L2 **L3**

*Synthesis of compound **L3***: **L2** (10.41 g, 20 mmol) and THF (150 mL) were added to a 500 mL round-bottom flask. To this stirred solution, a 150 mL THF solution of 1,3-dibromo-5,5-dimethylhydantoin (DBH; 14.30 g, 50 mmol) was slowly added at 0 ºC. The resulting mixture was then stirred at room temperature for 24 hours. After completion of the reaction, the mixture was poured into an aqueous sodium bisulfite solution, and the crude product was extracted with diethyl ether (3 × 50 mL). The combined organic extracts were washed with saturated brine, dried over anhydrous $MgSO_4$, filtered, and concentrated under reduced pressure. The crude residue was further purified by distillation to afford **L3** as a light-yellow solid (11.535 g, 85% yield). ^{1}H NMR (600 MHz, $CDCl_3$) δ (ppm): 8.60 (d, J = 8.9 Hz, 4H), 7.90 (d, J = 8.7 Hz, 4H), 7.60 (ddd, J = 8.5, 4.8, 1.4 Hz, 4H), 7.50 (ddd, J = 8.3, 6.6, 1.4 Hz, 4H), 6.93 (s, 1H), 4.14 (s, 3H), 3.54 (s, 6H). ^{13}C NMR (151 MHz, $CDCl_3$) δ (ppm): 152.92, 146.98, 133.65, 131.43, 130.47, 130.22, 128.23, 127.48, 127.09, 126.05, 123.34, 61.55, 61.26. APCI-HRMS: m/z calcd for $[M + H]^+$ $C_{37}H_{27}Br_2O_3^+$, 679.0306, found 679.0305, error −0.1 ppm.

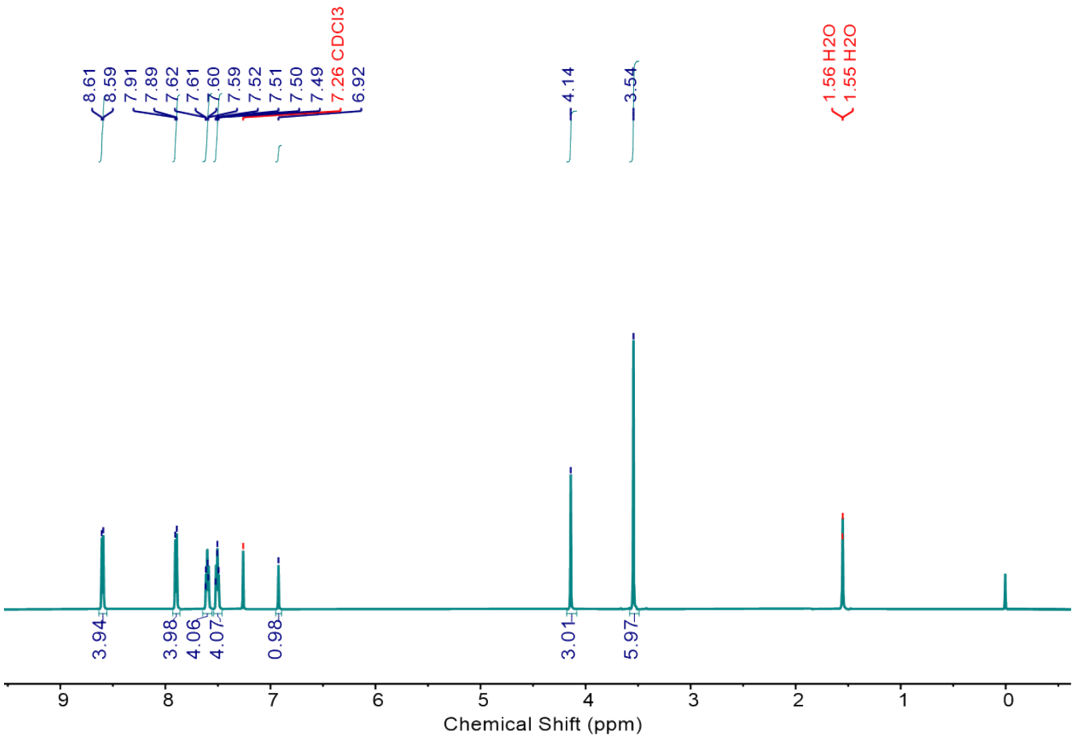

Fig. S9. The ^{1}H NMR spectrum (600 MHz, $CDCl_3$, 298 K) of **L3**.

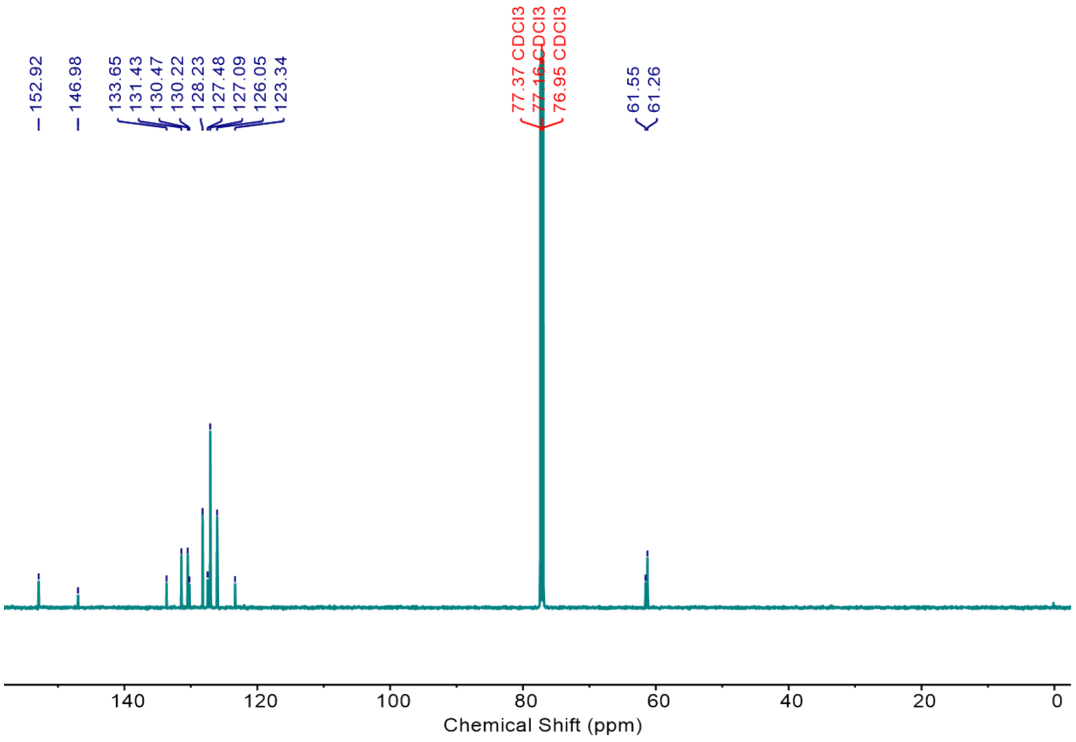

Fig. S10. The ^{13}C NMR spectrum (151 MHz, $CDCl_3$, 298 K) of **L3**.

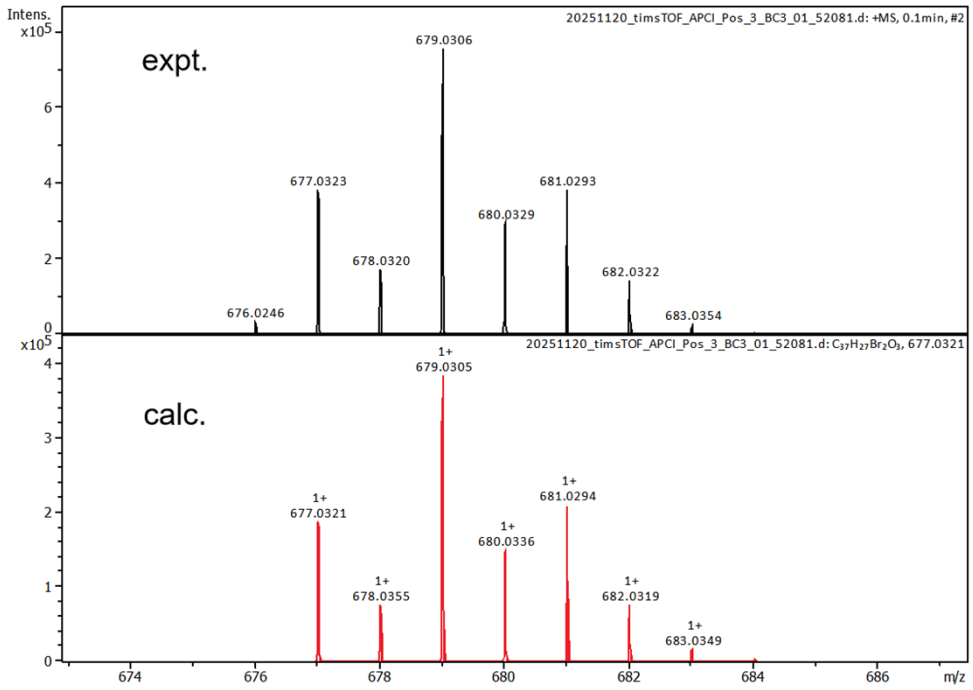

Fig. S11. APCI mass spectrum of **L3**.

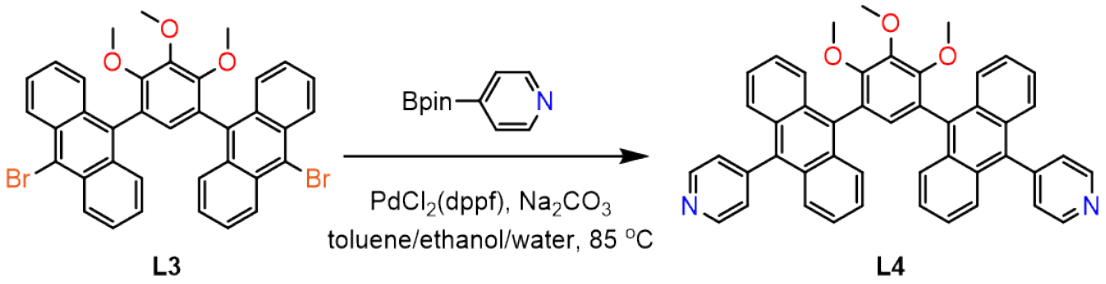

L3 **L4**

*Synthesis of compound **L4***: **L3** (6.78 g, 10 mmol), 4-pyridineboronic acid pinacol ester (5.13 g, 25 mmol), and anhydrous sodium carbonate (10.6g, 100 mmol) were dissolved in a mixed solvent of toluene (300 mL), ethanol (30 mL), and deionized water (30 mL). The mixture was thoroughly stirred with a magnetic stirrer until uniformly dispersed. Subsequently, [1,1'-bis(diphenylphosphino) ferrocene]dichloropalladium(II) ($Pd(dppf)Cl_2$; 732 mg, 1 mmol) was added as the catalyst. The reaction system was degassed by three cycles of evacuation and backfilling with nitrogen, with each cycle maintained for 20 minutes, to ensure a strictly inert atmosphere. The reaction mixture was heated to 85 °C in an oil bath and stirred continuously for 12 hours. After completion of the reaction, the organic solvent was removed by rotary evaporation

under reduced pressure. The resulting residue was washed with deionized water, and the aqueous phase was extracted with ethyl acetate (3 × 80 mL). The combined organic extracts were dried over anhydrous $MgSO_4$ and filtered. The filtrate was concentrated under reduced pressure to afford a crude product, which was further purified by silica gel column chromatography using a mobile phase of DCM/MeOH (30:1, v/v). This afforded compound **L4** as a light-yellow solid (6.475 g, 96% yield). ^{1}H NMR (600 MHz, CD_2Cl_2) δ (ppm) 8.86 (d, J = 5.0 Hz, 2H), 8.80 (d, J = 5.0 Hz, 2H), 8.00 (d, J = 8.8 Hz, 4H), 7.61 (d, J = 8.8 Hz, 4H), 7.52–7.49 (m, 6H), 7.41–7.36 (m, 6H), 7.01 (s, 1H), 4.17 (s, 3H), 3.63 (s, 6H). ^{13}C NMR (151 MHz, CD_2Cl_2) δ (ppm): 153.28, 150.43, 150.41, 147.79, 147.47, 134.58, 134.51, 130.57, 130.38, 129.59, 128.14, 127.31, 126.94, 126.69, 126.04, 125.86, 61.61, 61.45. APCI-HRMS: m/z calcd for $[M + H]^+$ $C_{47}H_{35}N_2O_3^+$, 675.2642, found 675.2643, error 0.1 ppm.

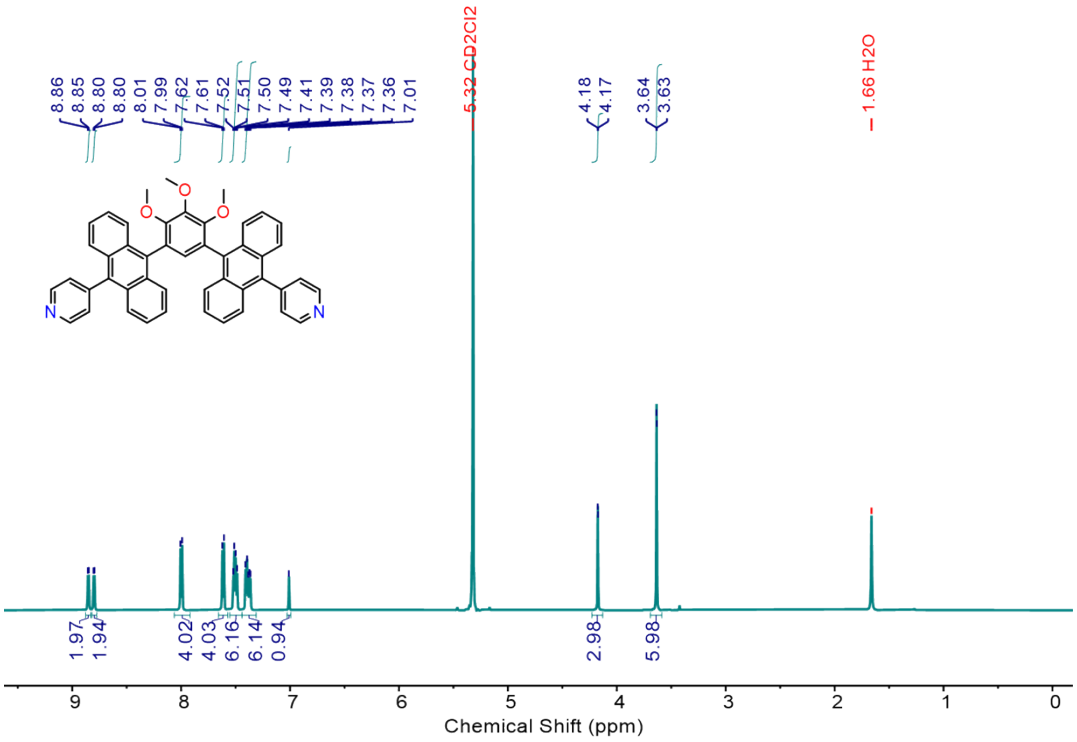

Fig. S12. The ^{1}H NMR spectrum (600 MHz, CD_2Cl_2, 298 K) of **L4**.

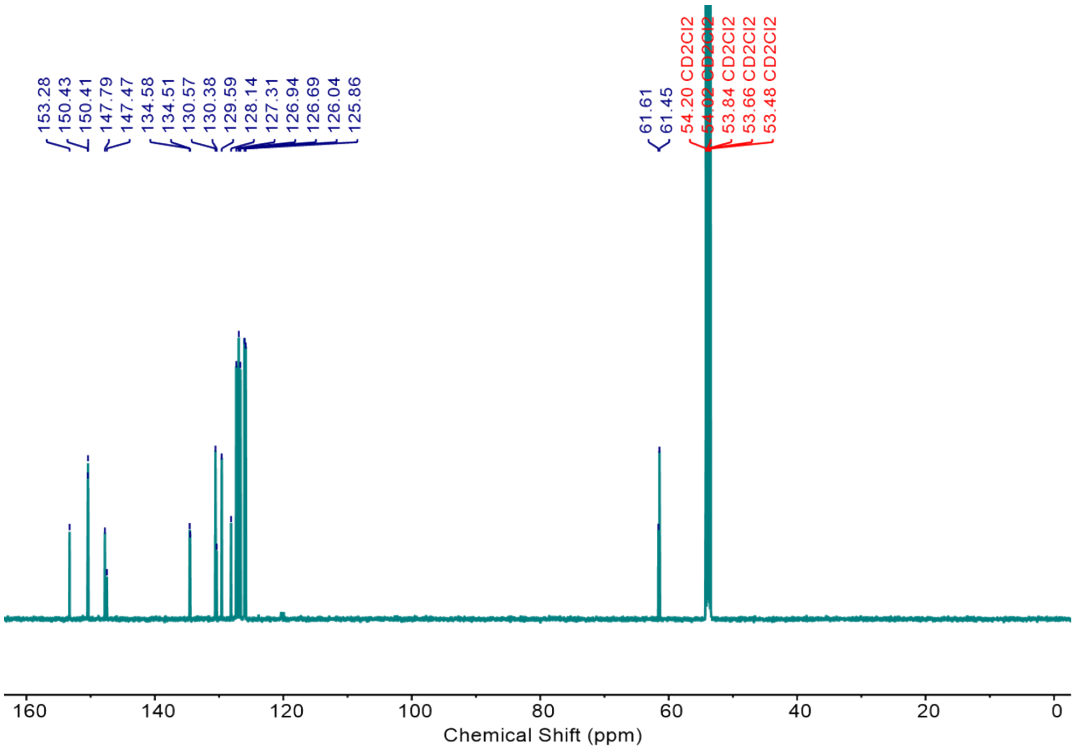

Fig. S13. The ^{13}C NMR spectrum (151 MHz, CD_2Cl_2, 298 K) of **L4**.

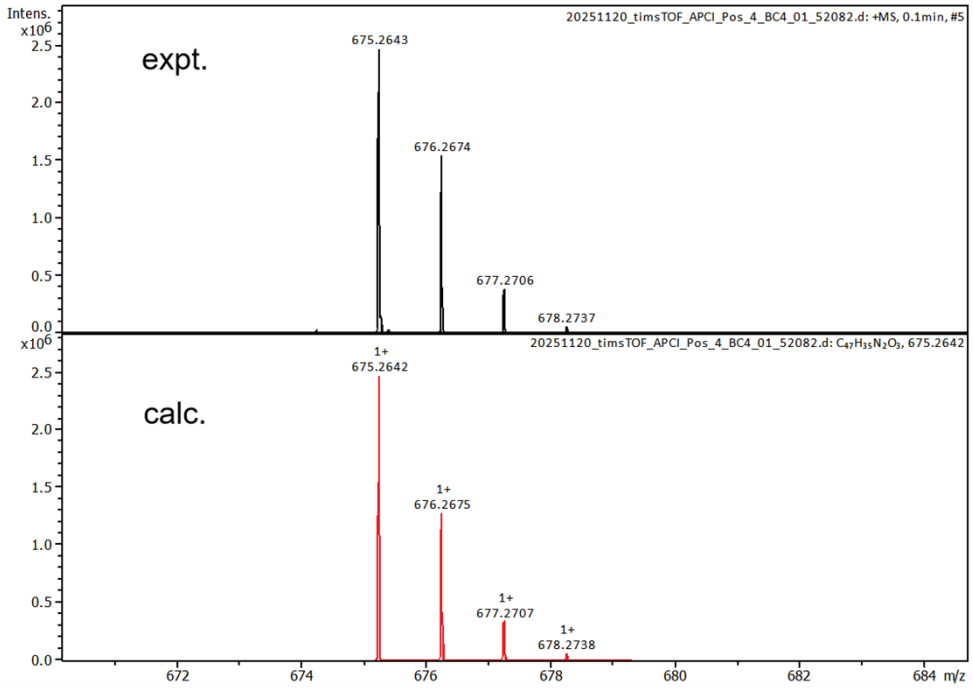

Fig. S14. APCI mass spectrum of **L4**.

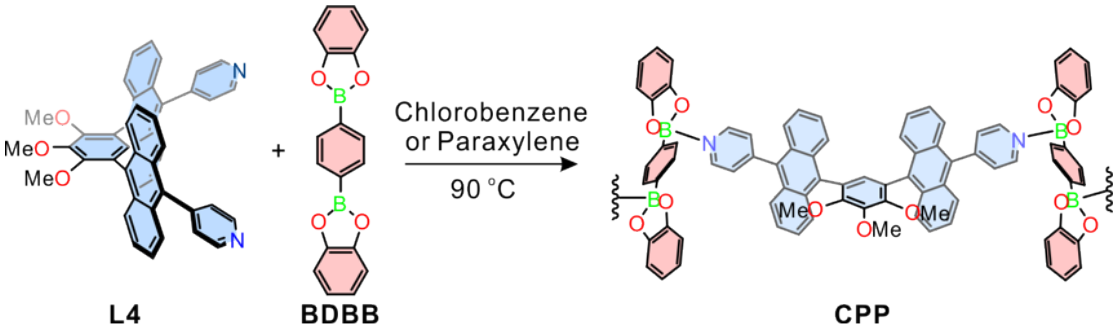

*Synthesis of **CPP***: **L4** (135 mg, 0.2 mmol) and **BDBB** (63 mg, 0.2 mmol) were added to clorobenzene or paraxylene (70 mL) and mixed using ultrasound for 15 min. The mixture was heated at 90 °C for 24 hours. The resulting solution was cooled slowly to room temperature. Colorless single crystals of **CPP** were obtained (185 mg, 93 %, m.p. > 250 °C.).

*4. Characterization and Computational Simulation of **CPP***

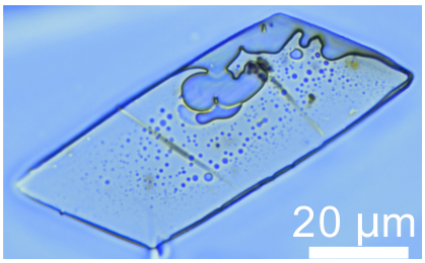

Fig. S15. Optical microscopy image of **CPP**.

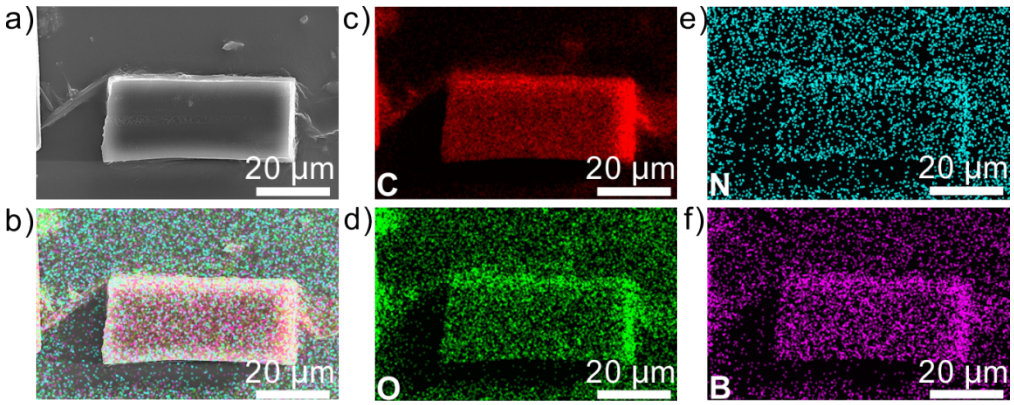

Fig. S16. SEM images (a) and the EDS mapping (b) of **CPP**. The corresponding elemental maps: carbon (c), oxygen (d), nitrogen (e), and boron (f).

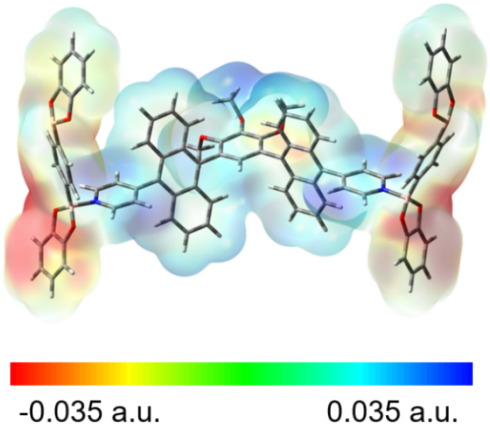

Fig. S17. Electrostatic potential surface of segment of **CPP** structure. Dative B–N bond results in the boronate moiety being negatively charged, while the **L4** is electron-deficient.

Table. S1: The calculation results of B–N bond energy

	Single-point energy	B–N·bond·energy
$\mathbf{E_{L4}}$	-2146.8609 hartree	-0.1635 hartree -214.7 kJ/mol
$\mathbf{E_{BDBB}}$	-1043.9479 hartree	
$\mathbf{E_{adduct}}$	-4234.9202 hartree	

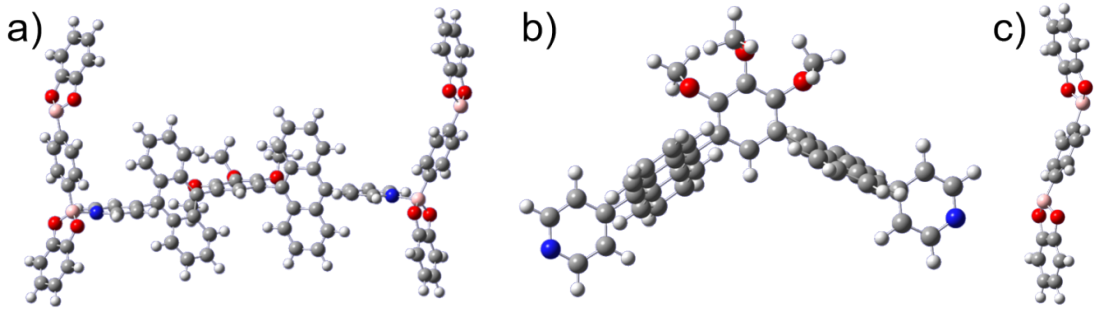

Fig. S18. Optimized conformation of a) **adduct**, b) **L4**, and c) **BDBB**.

5. X-Ray Single Crystallography Analysis

Table S2: Crystal data and structure refinement for **CPP-CB** and **CPP-PX**.

entry	**CPP-CB**	**CPP-PX**
Empirical formula	$C_{71}H_{51}B_2ClN_2O7$	$C_{105}H_{96}B_2N_2O7$
Formula weight	1101.21	1519.45
Temperature(K)	193	200
Crystal system	orthorhombic	monoclinic
Space group	*P*nma	$P2_1/c$
a(Å)	8.2913(7)	43.8807(6)
b(Å)	42.949(4)	24.9175(7)
c(Å)	25.2756(19)	8.31490(10)
α(°)	90	90
β(°)	90	94.5440(10)
γ(°)	90	90
Volume(Å^3)	9000.7(13)	9062.9(3)
Z	4	4
ρ_{calc}(g/cm^3)	0.813	1.114
μ(mm^{-1})	0.442	0.532
F(000)	2296.0	3224.0
Reflections collected	62784	62784
Independent reflections	8284 [R_{int} = 0.0879, R_{sigma} = 0.0580]	16051 [R_{int} = 0.0989, R_{sigma} = 0.0709]
Data/restraints/parameters	8284/1143/439	16051/334/1133
Goodness-of-fit on F^2	1.037	1.090
Final R indexes [I>=2σ (I)]	R_1 = 0.1760, wR_2 = 0.3608	R_1 = 0.0667, wR_2 = 0.1724
Final R indexes [all data]	R_1 = 0.2241, wR_2 = 0.3828	R_1 = 0.0925, wR_2 = 0.1857
CCDC number	2512776	2512777

CPP-CB:

PLAT082_ALERT_2_B High R_1 Value ..... 0.18 Report

PLAT084_ALERT_3_B High wR_2 Value (i.e. > 0.25) ..... 0.38 Report

PLAT340_ALERT_3_B Low Bond Precision on C-C Bonds ..... 0.01313 Ang.

Response: The crystal has too weak diffraction to obtain high resolution data. Correct atom identies, established by other chemical means.

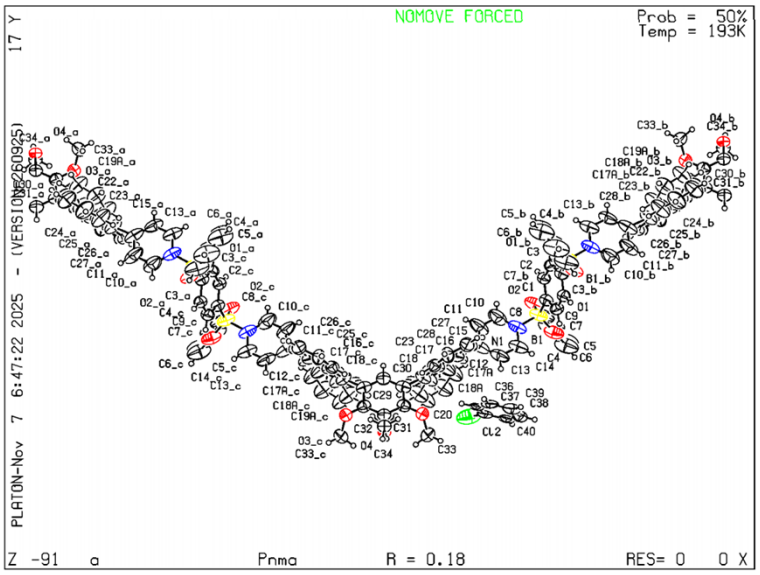

Fig. S19. Oak ridge thermal ellipsoid plot of **CPP-CB**.

CPP-PX: No A or B alerts

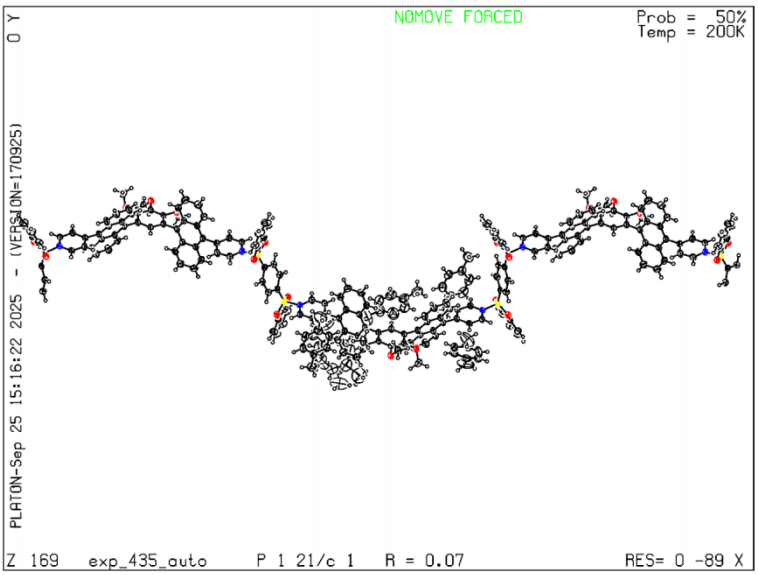

Fig. S20. Oak ridge thermal ellipsoid plot of **CPP-PX**.

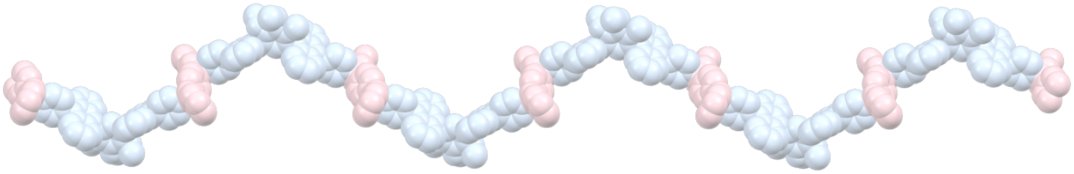

Fig. S21. The polymer chains in the **CPP-PX** crystal. The polymer chain conformation of **CPP-PX** is similar to that of **CPP-CB** in maintext.

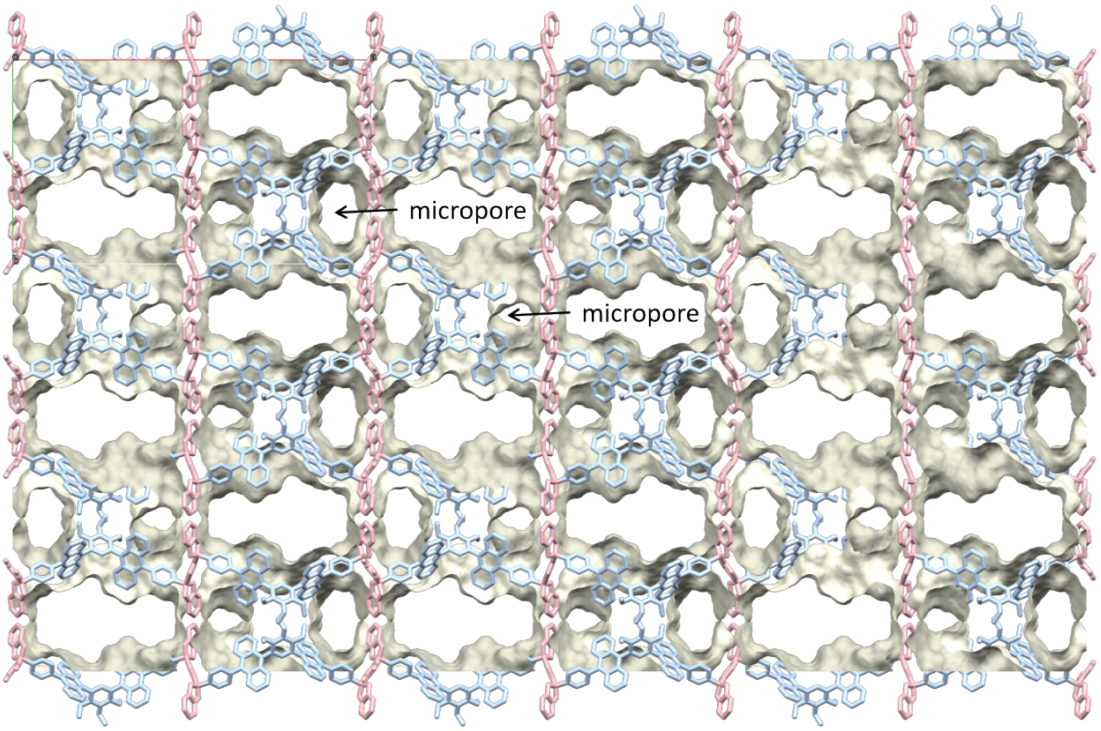

Fig. S22. The pore structure of **CPP-PX**.

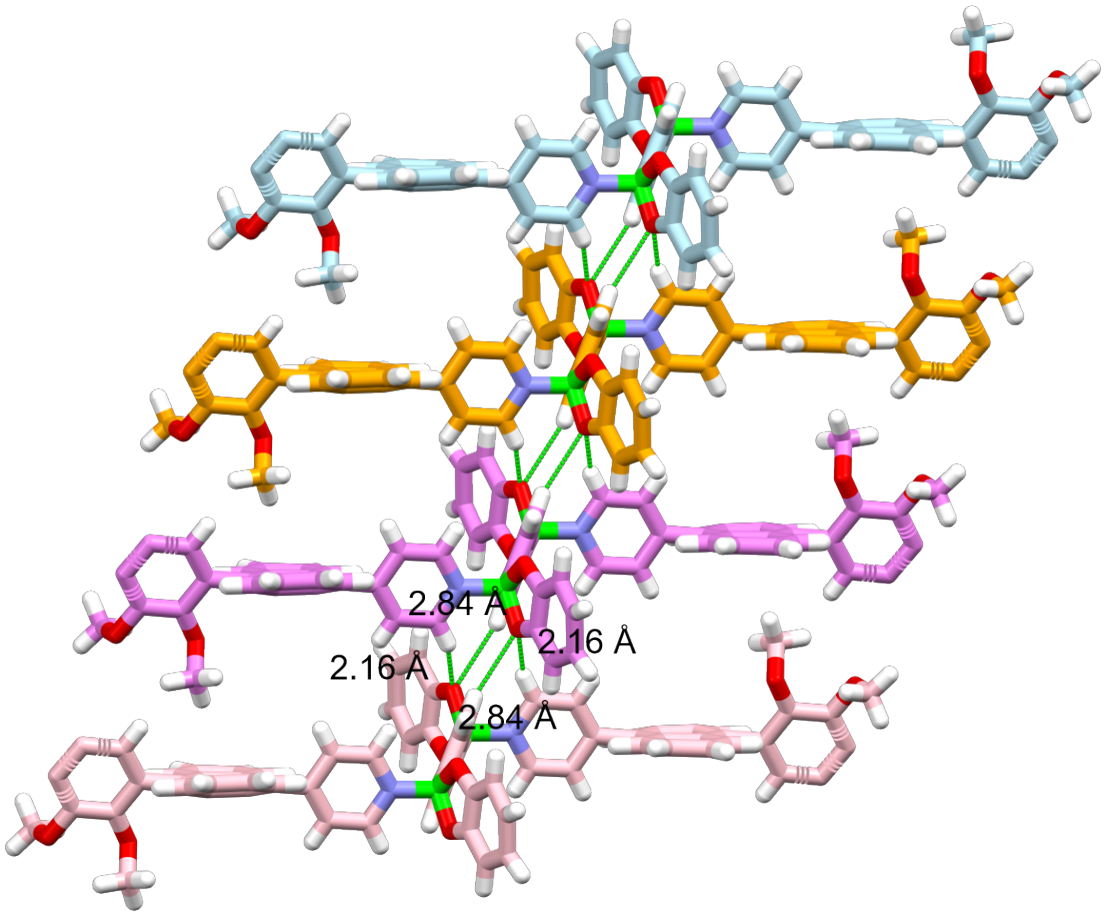

Fig. S23. The hierarchical assembly of dative polymer chains. Distinct polymer chains (differentiated by colors: light blue, orange, purple, and pink) undergo staggered stacking. In the boronate ester region, hydrogen bond tetramers are formed, as evidenced by the green dashed lines indicating hydrogen bonds with lengths of 2.16 Å and 2.84 Å. These tetramers further extend into a continuous hydrogen bond array, illustrating how the dative polymer chains self-assemble into a well-ordered supramolecular structure via hydrogen bonding and staggered stacking.

6. *Porous Properties of **CPP***

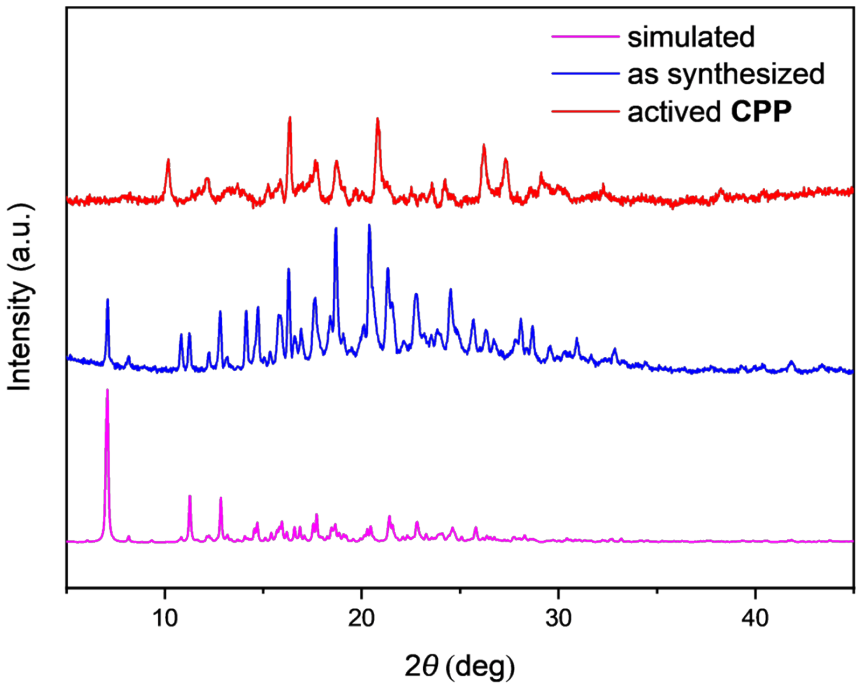

Fig. S24. PXRD patterns of simulated, as-synthesized and activated **CPP**.

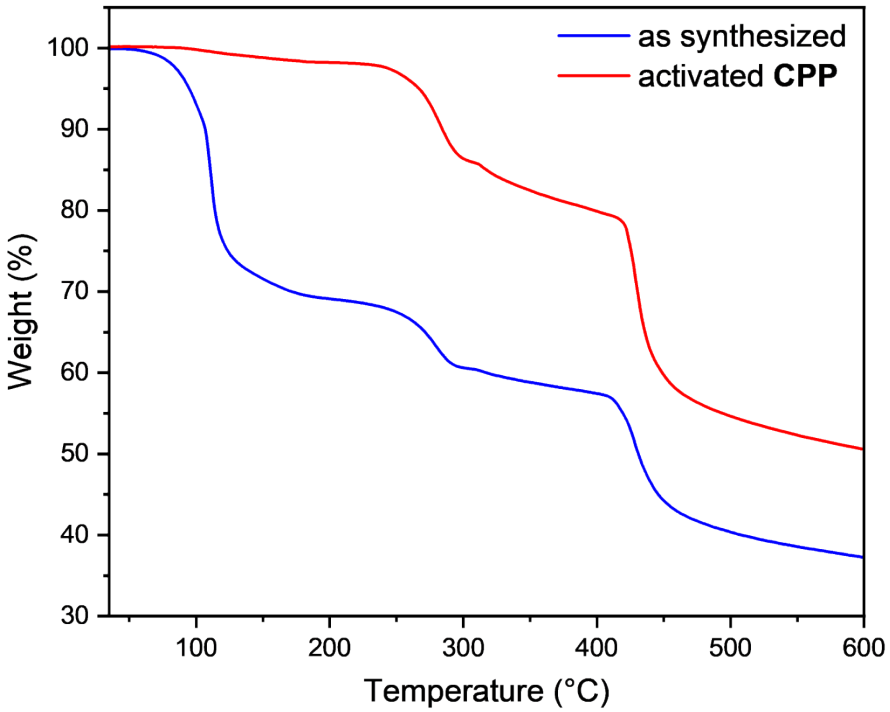

Fig. S25. Thermogravimetric analysis of as synthesized and activated **CPP**.

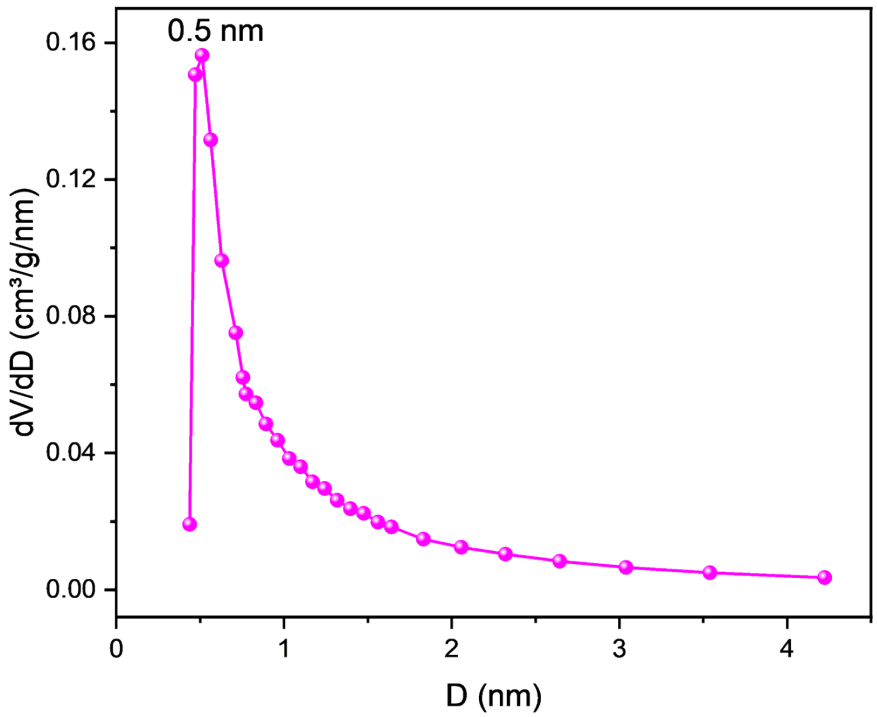

Fig. S26. Pore size distribution of **CPP-a** *via* the Horvath-Kawazoe method. Pore size distribution is concentrated in the range of 0.5–1 nm, consistent with those derived from crystal structure measurements.

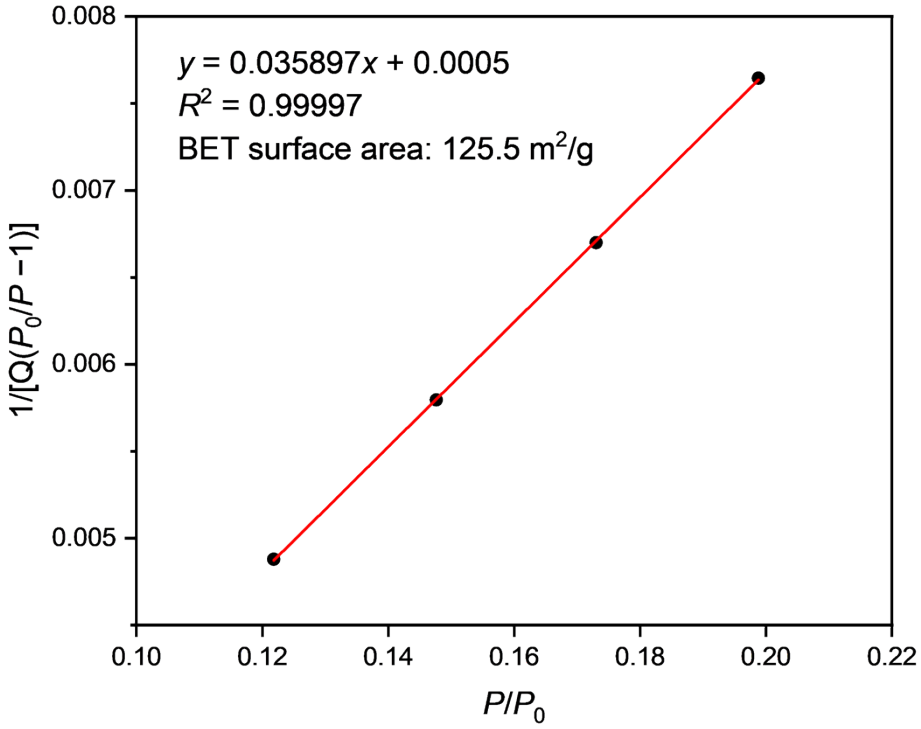

Fig. S27. BET multipoint fitting linear plot of **CPP-a**.

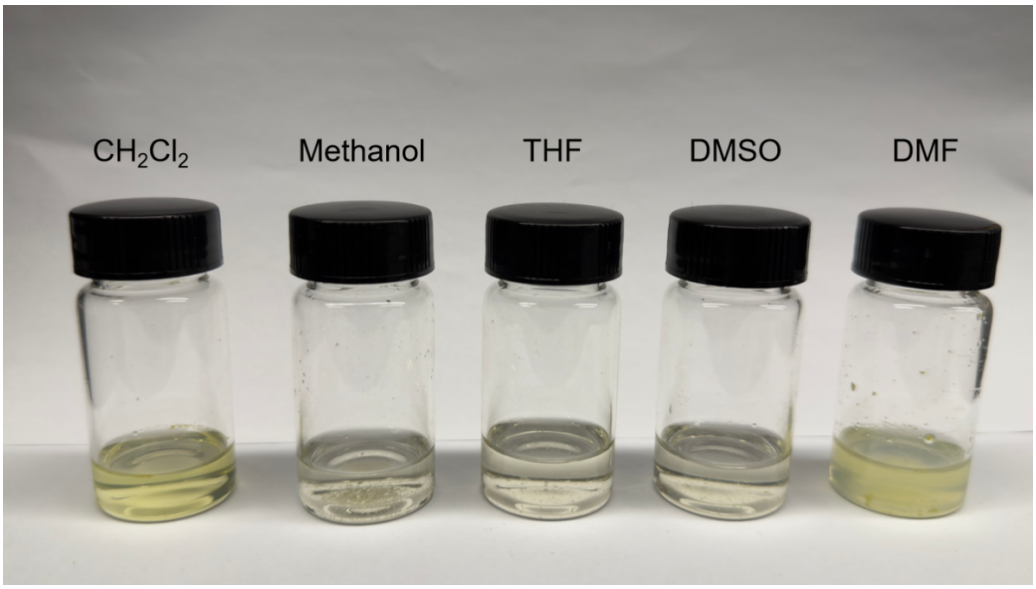

Fig. S28. Solubility behavior of 5 mg of **CPP-a** in 5 mL of dichloromethane, methanol, tetrahydrofuran, DMSO and DMF.

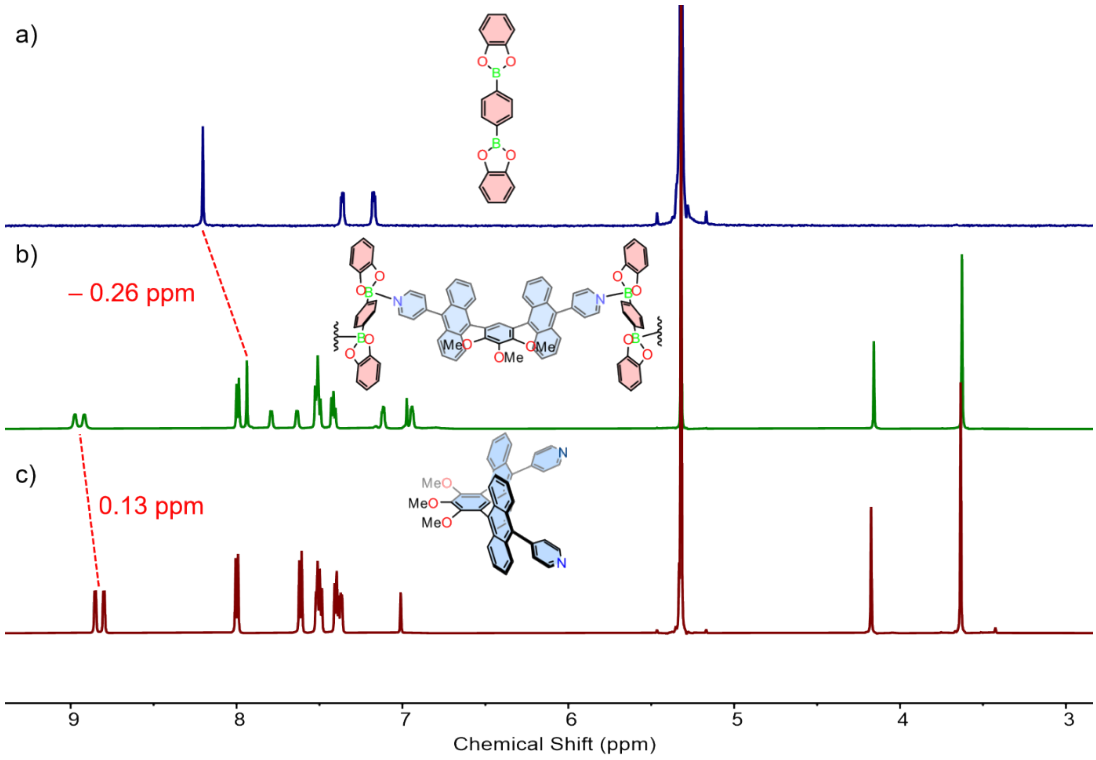

Fig. S29. ^{1}H NMR spectra (600 MHz, CD_2Cl_2, 298 K) of (a) **BDBB**, (b) **CPP-a**, and (c) **L4**. The pyridyl protons of the **L4** moieties shifted downfield, whereas the phenyl protons of the **BDBB** moieties shifted upfield, which suggests that dative B–N bonds may still exist in the solution phase. However, the proton peaks in the ^{1}H NMR spectrum of **CPP-a** are relatively sharp, without showing complex splitting patterns. This spectral feature is dissimilar to the broadened peaks typically characteristic of high polymers, and it also differs from the peak-splitting phenomena commonly observed in oligomers (e.g., tetramers, pentamers, hexamers, etc., which usually exhibit peak splitting due to symmetry-related effects). We therefore reason that **CPP-a** dissolved in CD_2Cl_2 still exists in a polymer-like form, whereas the dative B–N bonds between the **L4** and **BDBB** moieties undergo rapid exchange on the NMR time scale. Thus, the solution-phase behavior of **CPP-a** cannot be interpreted by analogy with its solid-state framework structure.

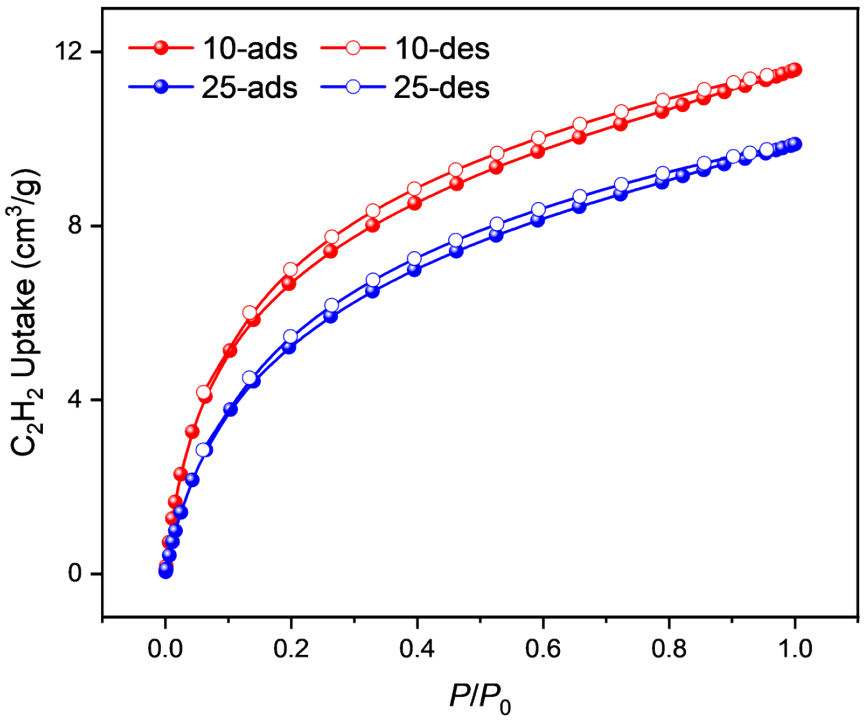

Fig. S30. The single-component C_2H_2 sorption isotherms of **CPP-a** at 283K and 298 K.

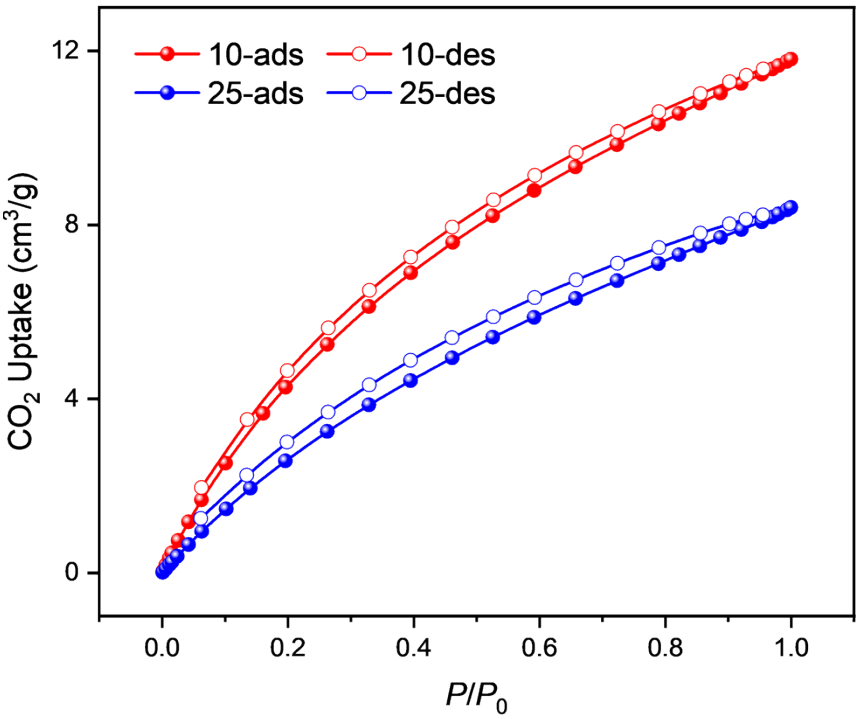

Fig. S31. The single-component CO_2 sorption isotherms of **CPP-a** at 283K and 298 K.

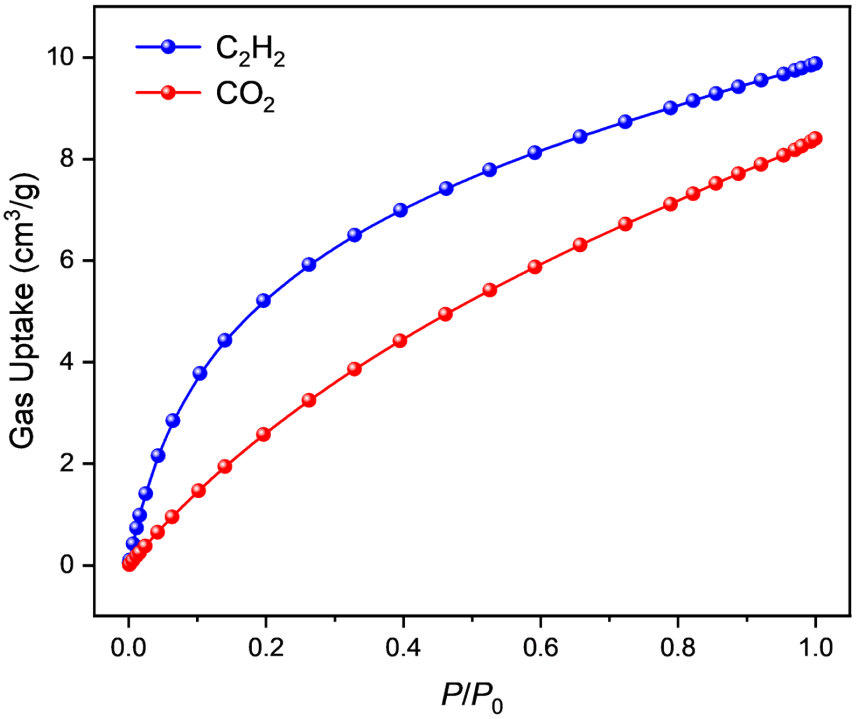

Fig. S32. C_2H_2 (blue) and CO_2 (red) adsorption isotherms of **CPP-a** at 298 K.

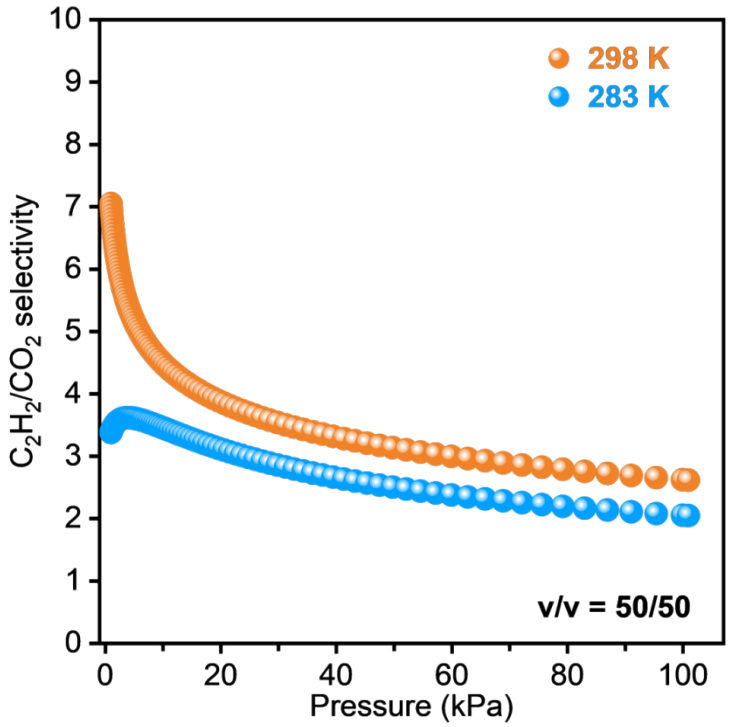

Fig. S33. The calculated IAST selectivity of C_2H_2/CO_2 at 283K and 298 K.

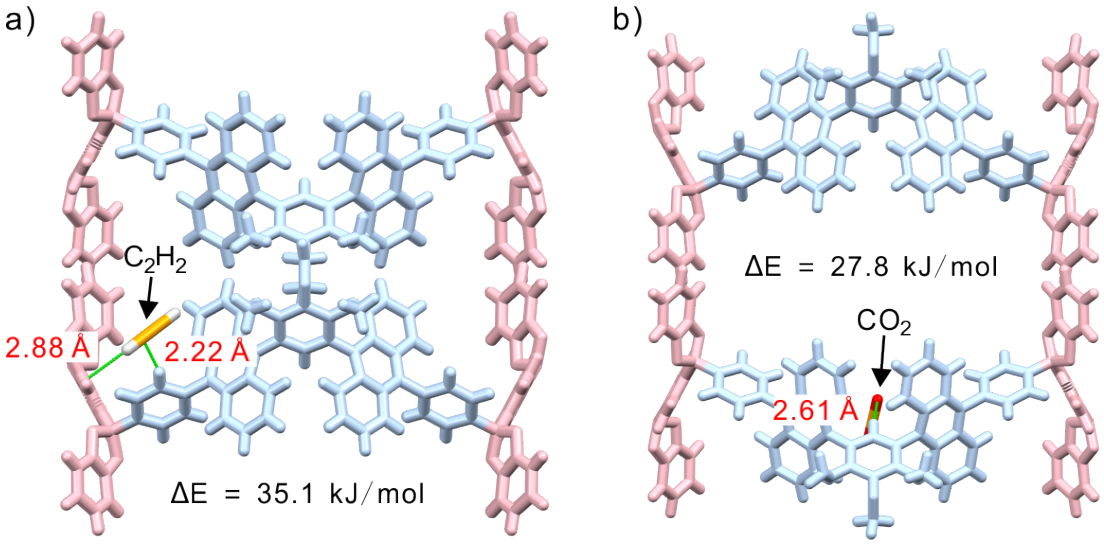

Fig. S34. (a) C_2H_2 and (f) CO_2 optimal binding site within the pore of **CPP-a**.

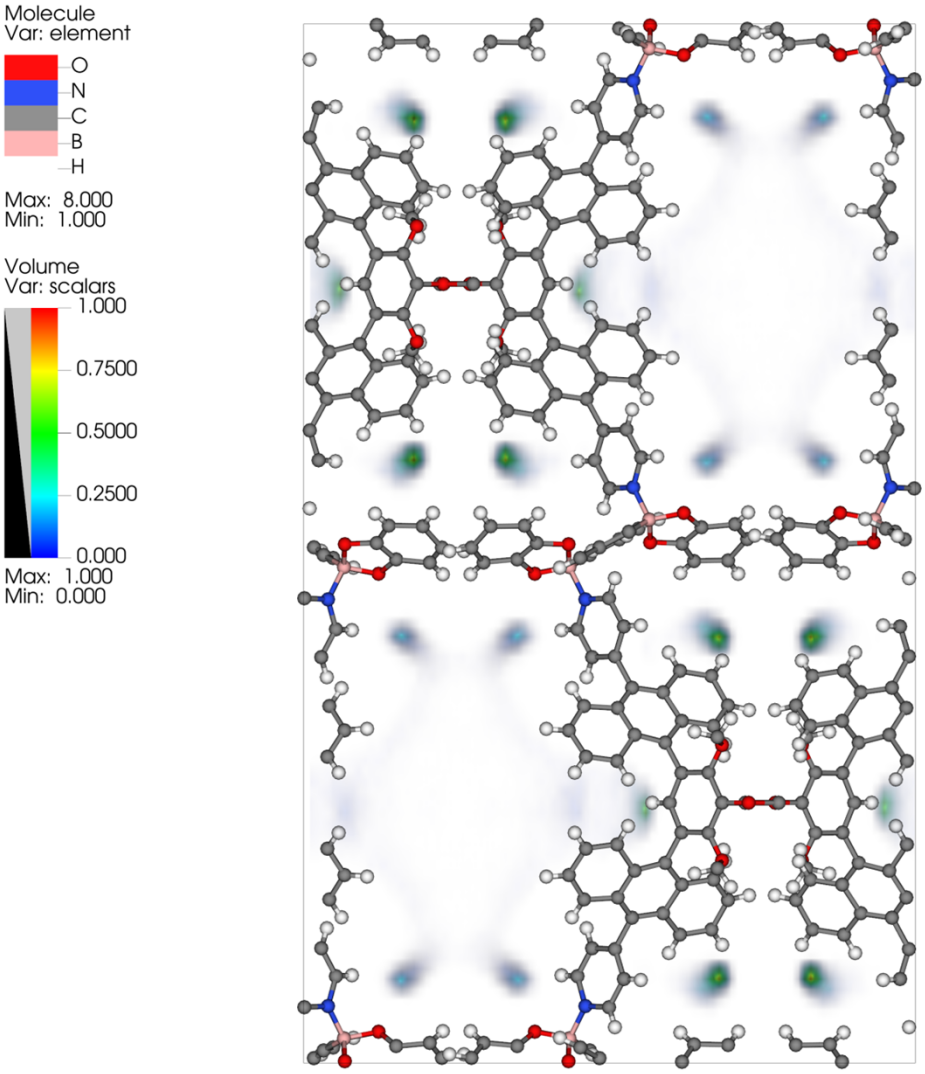

Fig. S35. C_2H_2 density distribution calculated by GCMC simulations for **CPP-a**.

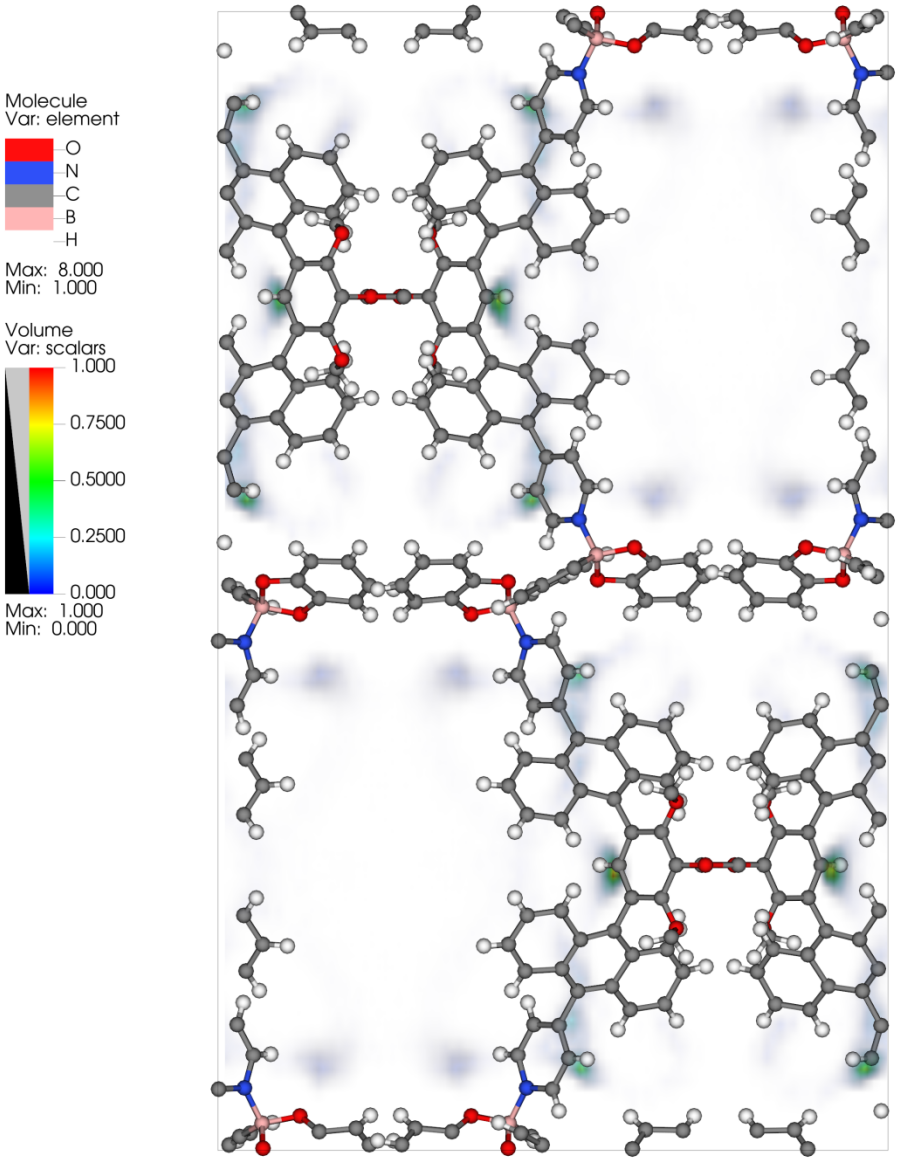

Fig. S36. CO_2 density distribution calculated by GCMC simulations for **CPP-a**.

Reference

1. Sheldrick, G. M. *Acta Cryst.* **C71**, 3−8 (2015).
2. Dolomanov, O. V., Bourhis, L. J., Gildea,R. J., Howard, J. A. K. & Puschmann, H. J. *Appl. Cryst.* **42**, 339−341 (2009).
3. Spek, A. L. *Acta Crystallorgr.* **C71**, 9−18 (2015).
4. Neese, F. *WIREs Comput. Mol. Sci.* **8**, e1327 (2018).
5. Becke, A. D. *J. Chem. Phys.* **98**, 5648−5652 (1993).
6. Hariharan, P. C., Pople, J. A. *Theor. Chim. Acta* **28**, 213−222 (1973).
7. Zhou, Y. et al. *J. Phys. Chem. B* **117**, 11709−11718 (2013).
8. Lu, T. & Chen, F. *J. Comput. Chem.* **33**, 580−592 (2012).
9. Lu, T. *J. Chem. Phys.* **161**, 082503 (2024).
10. Grimme, S., Ehrlich, S., Goerigk, L. *J. Comput. Chem.* **32**, 1456−1465 (2011).
11. Humphrey, W., Dalke, A. & Schulten, K. *J. Mol. Graph.* **14**, 33−38 (1996).
12. Myers, A. L. & Prausnitz, J. M. *AIChE J.* **11**, 121−127 (1965).
13. Metropolis, N., Rosenbluth, A. W., Rosenbluth, M. N., Teller A. H. & Teller, E. *J. Chem. Phys.* **21**, 1087−1092 (1953).
14. Mayo, S. L., Olafson B. D. & Goddard, W. A. *J. Phys. Chem.* **94**, 8897−8909 (1990).
15. Ewald, P. P. *Ann. Phys.* **369**, 253−287 (1921).
16. Potoff J. J. & Siepmann, J. I. *AlChE J.* **47**, 1676−1682 (2001).
17. Delley, B. *J. Chem. Phys.* **113**, 7756−7764 (2000).
18. Perdew, J. P., Burke K. & Ernzerhof, M. *Phys. Rev. Lett.* **77**, 3865-3868 (1996).